



UNIVERSITY OF LEEDS

This is a repository copy of *Automated In Silico Energy Mapping of Facet-Specific Interparticle Interactions*.

White Rose Research Online URL for this paper:

<https://eprints.whiterose.ac.uk/194226/>

Version: Accepted Version

---

**Article:**

Moldovan, AA [orcid.org/0000-0003-2776-3879](https://orcid.org/0000-0003-2776-3879), Penchev, RY, Hammond, RB [orcid.org/0000-0003-0691-7779](https://orcid.org/0000-0003-0691-7779) et al. (4 more authors) (2021) Automated In Silico Energy Mapping of Facet-Specific Interparticle Interactions. *Crystal Growth and Design*, 21 (10). pp. 5780-5791. ISSN 1528-7483

<https://doi.org/10.1021/acs.cgd.1c00674>

---

© 2021 American Chemical Society. This is an author produced version of an article published in *Crystal Growth and Design*. Uploaded in accordance with the publisher's self-archiving policy.

**Reuse**

Items deposited in White Rose Research Online are protected by copyright, with all rights reserved unless indicated otherwise. They may be downloaded and/or printed for private study, or other acts as permitted by national copyright laws. The publisher or other rights holders may allow further reproduction and re-use of the full text version. This is indicated by the licence information on the White Rose Research Online record for the item.

**Takedown**

If you consider content in White Rose Research Online to be in breach of UK law, please notify us by emailing [eprints@whiterose.ac.uk](mailto:eprints@whiterose.ac.uk) including the URL of the record and the reason for the withdrawal request.



[eprints@whiterose.ac.uk](mailto:eprints@whiterose.ac.uk)  
<https://eprints.whiterose.ac.uk/>

# Automated In-Silico Energy Mapping of Facet Specific Inter-Particle Interactions

*Alexandru A. Moldovan<sup>†,1,\*</sup>, Radoslav Y. Penchev<sup>‡</sup>, Robert B. Hammond<sup>§</sup>, Jakub P. Janowiak<sup>†</sup>, Thomas E. Hardcastle<sup>†,1</sup>, Andrew G. P. Maloney<sup>1</sup>, and Simon D. A. Connell<sup>⊥,\*</sup>*

<sup>†</sup> Center for Doctoral Training, Complex Particulates Products and Processes, School of Chemical and Process Engineering, University of Leeds, Leeds, UK

<sup>‡</sup> Pfizer, Sandwich, Kent, UK

<sup>§</sup> School of Chemical and Process Engineering, University of Leeds, Leeds, UK

<sup>||</sup> Cambridge Crystallographic Data Centre, Cambridge, UK

<sup>⊥</sup> School of Physics and Astrophysics, University of Leeds, Leeds, UK

Key Words: Crystal Engineering, Surface Interactions, Surfaces, Formulations, Inter-particulate, Particle-particle Interactions, Surface Chemistry, Atomistics Modelling

## Abstract

Particle-particle interactions impact the processability and performance of drug products. Faceted particulates exhibit distinct surface chemistries which affect their adhesion causing downstream processing challenges such as poor flow, punch sticking, and compaction. Currently there is a lack of tools to assist formulators in predicting these challenges based on particle properties. Here we present a methodology for navigating the energy landscape of inter-particle interactions. We used molecular mechanics to calculate the interactions between slabs of molecules representing distinct facets. The workflow enables a rapid assessment of the total energy landscape between interacting particles, providing insight into the effects of different surface chemistries and molecular topologies. Previously, the strongest interaction (lowest energy) was used to

calculate the propensity to adhere, but we demonstrate that this does not always predict an accurate description of the likely surface interactions. We chose paracetamol to demonstrate the application of this methodology. The most cohesive facets were the (101) and (10-1). Comparing surface interactions between particles allows a ranking of the most energetically compatible surfaces. The significance of this ranking and understanding how the surface chemistry can impact inter-particle interactions is a step towards assisting formulation decisions, and improvements in product performance.

## Introduction

Due to recent advances in manufacturing technology and encouraged by regulatory bodies<sup>1</sup> the pharmaceutical companies are making significant investments in continuous processing<sup>2-4</sup> in order to benefit from improved product quality, easier scale up and lower development costs.

Continuous manufacturing, however, is much more sensitive to powder properties compared to the traditional batch manufacturing. Most critical to the seamless production of Oral Solid Dosage forms using continuous processing is the ability of the Drug Substance (DS) powder and Drug Product (DP) blend to flow well. The flowability of powders depends on a number of factors with particle shape and particle size being the first one to be optimised, usually via a trial and error approach. The effect of particle shape on powder flow arises from both the physical and chemical interactions of the particles. Particles shapes are characterised by a set of crystallographic faces which are defined by their miller indices and relative surface areas. The different faces can often exhibit a significant difference in their surface chemistry depending on the molecular and crystallographic symmetries present. The surface chemistry is manifested in the magnitude of the cohesive (API-API or excipient-i-excipient-i) and adhesive (API-excipient or excipient-i -excipient-j) particle interactions and has been reported to have a significant impact on powder processability including flowability, compaction, and punch sticking<sup>5-7</sup>.

An effective way to anticipate or fix potential processing issues related to unfavourable particle cohesive/adhesive interactions is to adopt an in-silico crystal morphology screening to run “what-if” scenarios. A crystal engineering approach in accordance with the Materials Science Tetrahedron (MST) framework<sup>8</sup> can then also be employed to manipulate the morphology of the DS crystals and steer it toward one that provides more favourable particle-particle interactions.

Recent advances in computational hardware, improvements in the ab-initio calculations of the intermolecular interactions, and the availability of software with customizable workflow provide the pharmaceutical scientist with the ability to develop and implement their own models and computational workflows. This has led to a shift from the traditional trial and error by experimentation way of working

Modern computational tools have made in silico workflows a viable option for the pharmaceutical scientist. These new workflows are becoming embedded into drug development workflows alongside traditional experimental techniques. This combined way of working is encouraged by regulatory bodies<sup>9</sup> and backed by significant government funding.

Models have been developed to investigate surface interactions using molecular probes<sup>10,11</sup>, using a systematic search method where a single probe molecule, having three translational and three rotational degrees of freedom, is placed on a 3D grid above a slab and the interaction energy between the two calculated at every grid point and rotation. This method has been applied in a study of the cohesive-adhesive balance (CAB) for inhalation formulations and has compared well to experimental results<sup>12</sup>. Whilst this systematic search method was useful in mapping the interaction between the two bodies, representing the second surface as a molecule omits contributing interactions from the bulk of the slab at slightly longer range, thus ignoring a large percentage of atoms that could impact the overall adhesion of the two surfaces. A potentially larger effect is the omission of molecules laterally, which will also interact with the opposing surface and influence the probability that a probe molecule could approach at that particular position in 3D space, or rotation. This effect has been shown in a systematic grid search of two nano-clusters of ascorbic acid and aspirin<sup>11,13</sup> where the corners and edges were identified as highly energetic binding sites. However, the size of each cluster was not large enough to ensure convergence of energy, showing that bulk interactions and/or longer range lateral interactions were a significant contribution to total interaction energy.

In this work we present a computational model for the automated calculation of the interactions between pair of crystalline faces using four degrees of freedom. The model explicitly considers both surfaces of interest and thus overcomes some of the limitations inherent to estimating the interaction strength between two faces by using one face only and a single molecule as a proxy for the second face<sup>12</sup>.

Alongside the model, we have also developed a tool to aid in the analysis and automation of the facet specific interaction energy mapping. We used paracetamol as a case study to illustrate how the model works.

## Methodology

### Geometry Optimisation and Crystal Morphology

The crystal structure of paracetamol (Para)<sup>14</sup> was chosen as a case study and imported from the CSD (Cambridge Structural Database)<sup>15</sup> (CSD Refcode HXACAN28). All computational results were obtained using Dassault Systemes BIOVIA Materials Studio package<sup>16</sup>. Geometry optimisation was performed using the Forcite module. The pairwise intermolecular calculations were carried out using the Dreiding forcefield with atomic point charges calculated by MOPAC<sup>17</sup> using AM1<sup>18</sup>. Ewald summation was used for the electrostatic contribution with a buffer width of 0.5 Å and a limiting radius of 18.5 Å. A rigid body approximation was applied to the optimisations of the cell dimensions and hydrogen atom positions. The fit of a forcefield was judged by the closeness between the calculated lattice energy and experimental enthalpy of sublimation for paracetamol form (I) (28.26 kcal mol<sup>-1</sup>)<sup>19</sup> and the smallest deviation in geometry from the original structure (Supporting Information Table S1).

The morphology of paracetamol was calculated using the attachment energy<sup>20</sup> model within the Morphology module of Materials Studio with the same forcefield and summation parameters used in the geometry optimization step and a minimum d-spacing ( $d_{hkl}$ ) set to 0.8 Å. The anisotropy factor was calculated in order to approximate the saturation of unsatisfied surface intermolecular bonds<sup>21</sup>.

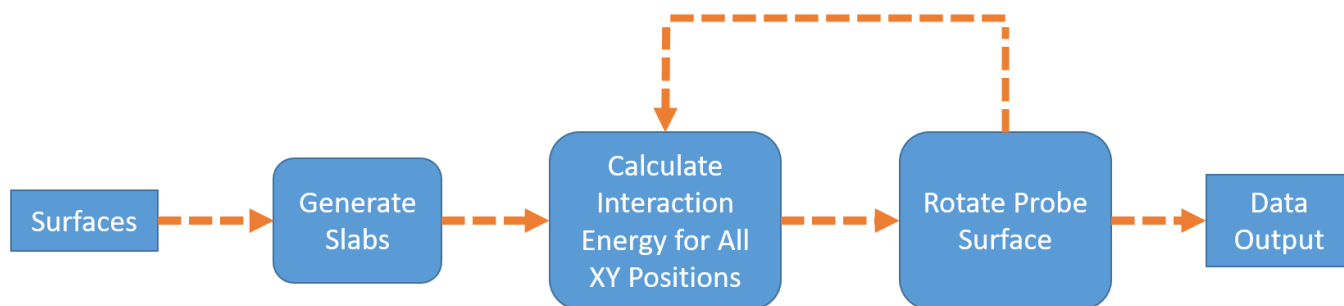


Figure 1- Workflow illustrating a high level overview of how the surface-surface interaction model (SSIM) calculates the interaction between two surfaces.

The workflow in Figure 1 describes the calculation of the interaction between two crystalline faces. Surfaces generated by the crystal morphology module were used to construct the interacting slabs. The interaction energy between the two slabs was calculated by minimising the energy between them. A systematic grid approach was taken to calculate the energy values for all XY positions. The probe surface was then rotated around the Z-axis and the processes repeated until all unique positions were calculated. No tilt is introduced into the probe or substrate surface, as such all calculations are carried out for parallel surfaces. To resolve lattice-mismatching across different systems, the surfaces-surface interactions were computed without the use of periodic boundary conditions. The code for this model can be found at this link (<https://gitlab.com/AlexAMC/ssim>).

While the attachment energy model was used to generate a morphology for the process outlined above, the model proposed is independent of the input morphology and as such is extensible to other morphology methods or experimental morphologies.

### 1. Generation of Interacting Layers

Slabs were generated to represent crystalline facets. Differences in the lattice parameters of periodic slabs resulted in supercells containing interacting slabs being prohibitively large. For this reason, pseudo-periodic supercells were used.

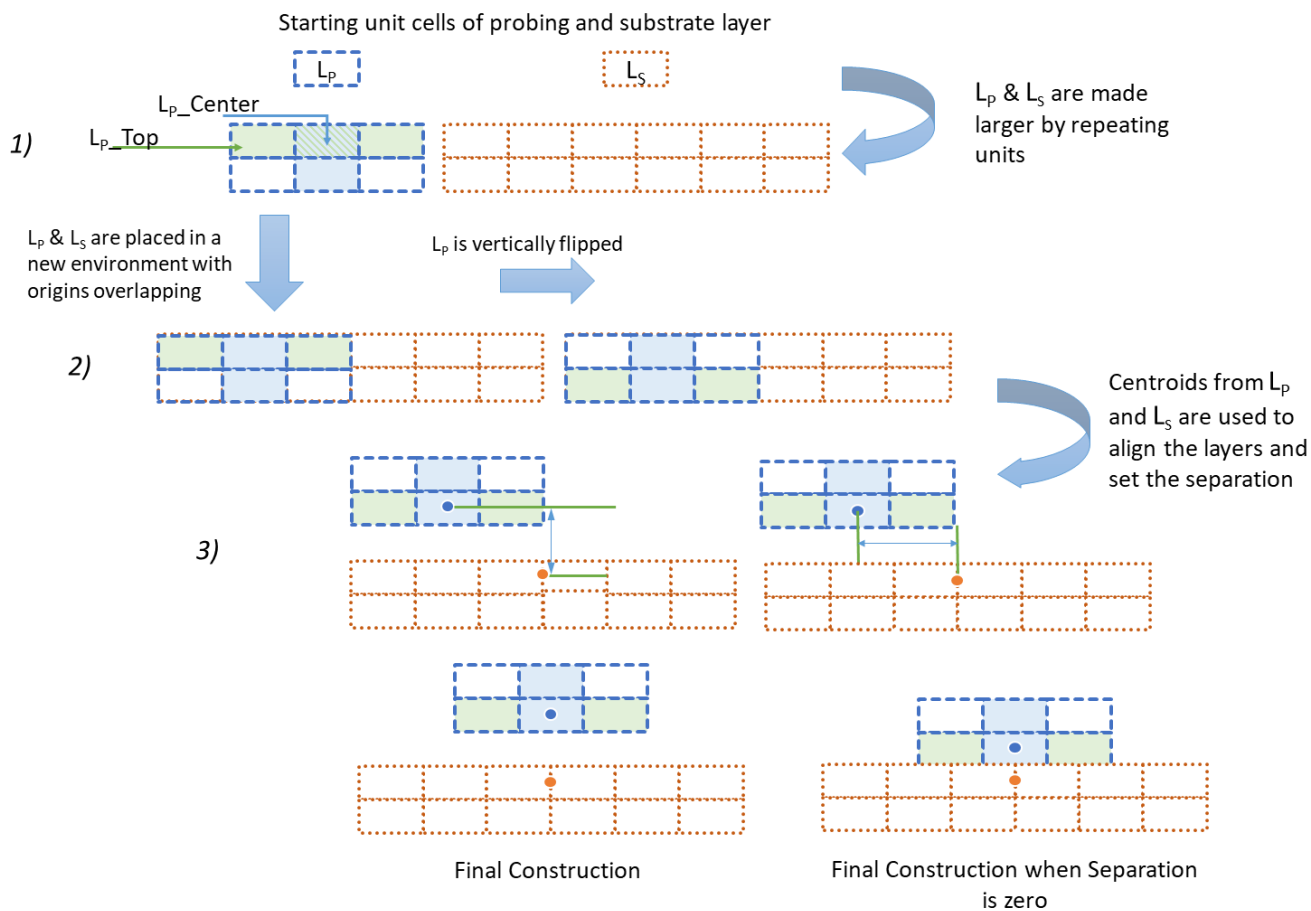


Figure 2 - Diagram illustrating the three steps required to construct the probing ( $L_p$ ) and substrate ( $L_s$ ) layers.

The construction and alignment of the pair of slabs representing the crystal surfaces of interest is outlined below and illustrated in Figure 2. The probe layer ( $L_p$ ) and substrate layer ( $L_s$ ) were generated from the faces calculated by the crystal morphology module as three-dimensional slabs.

Step 1) – Super cells of  $L_p$  and  $L_s$  were created using the surfaces generated from the morphology prediction.  $L_p$  requires dimensions of  $3 \times 3 \times T$ , where  $T$  is the number of unit cells required to achieve optimal thickness.

Calculated surfaces were rotated to align with the XY plane and their origins overlaid to facilitate construction of slabs. Optimum  $T$  for a specific system is obtained by increasing the slab thickness at  $d$ -spacing increments.

The thickness of the surface is measured from the cleave plane to the next equivalent plane. The default cleaving rules were applied for calculating the surface termination which states that atoms connected to molecules whose centroid are within the boundary are included in the slab.

While only one unit cell of  $L_P$  (labelled  $L_P\_Center$  in Figure 2) was required to calculate the interaction per unit area, the extra atoms around the primary central cell were used to detect any collision against  $L_S$  which might sit outside of the unit area.

In order to reduce the computational time all atoms in the  $L_P$  were fixed upon initial layer construction except those present in  $L_P\_Center$ . Pairwise interactions between fixed atoms does not contribute towards total energy calculations, as shown in Figure S1. The atoms present in the top d-spacing of  $L_P$  were used for detecting collisions between slabs (labelled  $L_P\_Top$  in Figure 2, cells highlighted in green).

The surface cell vectors  $U_S$  and  $V_S$  were multiplied by the minimum number of repeating units to construct  $L_S$ , an approximate square of the desired area set by convergence testing,  $A_{set}$ . The multiplication factor  $x_d$  for each unit cell dimension ( $U_S$  and  $V_S$ ) being calculated for  $A_{set}$  and  $L_d$  is the length of unit cell dimensions ( $U_S$  and  $V_S$ ) and is shown in Equation 1. A square approximation was used to resolve edge effects caused by high aspect ratio unit cells. The reticular area of the unit cell and slab are recorded for both layers to be used during normalisation for analysis.

$$x_d = \left\lceil \frac{\sqrt{A_{set}}}{L_d} \right\rceil \quad \text{Equation 1}$$

Step 2) - Due to the surface sampling method outlined below, the location of the initial starting point during construction for  $L_P$  and  $L_S$  is arbitrary. Both  $L_P$  and  $L_S$  were placed such that their origins overlapped. In order to ensure the two faces of interest were facing one another, the  $L_P$  was vertically flipped.

Step 3 ) Centroids of the top d-spacing of the two slabs were calculated (blue/orange dots in Figure 2). The two slabs were aligned in the XY plane and then separated along the Z-axis utilising the two centroids. The displacement distance  $D_{L_P-L_S}$  was calculated using Equation 2, where  $x_{sep}$  is the desired separation between the two slabs;  $T_P$  and  $T_S$  are the thicknesses of each slab.

$$D_{P-L} = x_{sep} + \left( \frac{T_P}{2} + \frac{T_S}{2} \right) \quad \text{Equation 2}$$

Centroids for each slab were generated in the top layers, thus their position remaining constant during convergence testing of the slab thickness.

The 3D grid for the  $L_P$  translations was calculated by taking the largest  $U_S/U_P$  and  $V_S/V_P$  vector from the two layers creating a grid large enough to encompass all unique points.

## 2. Interaction calculations

The interaction energy between two surfaces is defined as the summation of the repulsive and attractive interactions between atoms from each surface. A larger/stronger interaction energy will be noted as one that is more negative in value from here on in.

Once the slabs were constructed, the energy of  $L_P$  was calculated in isolation with  $L_P\_Center$  unfixed, and  $L_P\_Top$  fixed. The isolated environment allows for the internal slab energies to be calculated ( $E_P$  and  $E_S$ ), which were then used to calculate the interaction energy between the two slabs, as shown in Equation 3. The system energy ( $E_{sys}$ ) was calculated at every z-step during the scanning phase.

$$E_{int} = E_{sys} - (E_P + E_S) \quad \text{Equation 3}$$

A flow chart of the steps used to calculate the interaction between two surfaces is shown in Figure 3.

To decrease the computational time, the state of the atoms being fixed had to be controlled. Two modes were implemented. Firstly, the “collision detection” mode where the atoms in  $L_P\_Center$  were fixed while those in  $L_P\_Top$  were unfixed to enable any collisions to be detected between the two slabs. Secondly, the “interaction calculation” mode where the  $L_P\_Center$  and  $L_P\_Top$  fixed states were swapped. Due to the time requirement of switching between fixed states of the atoms, calculations were ran in batches of “collision detection” and “interaction calculations” thus giving a 10 fold reduction in time (on 4-cores Intel i7-4770k 3.8GHz). Illustration of the construction can be seen in Figure S1.

In “collision detection” mode, the energy minimum search was performed in the Z-direction, utilising the steepest descent method (further description in Figure S3). The energy minima were found and their XYZ positions were stored. Once the process was completed for all XY positions, the energy of the system was calculated at each of the XYZ points with “interaction calculation” enabled. By calculating  $E_{int}$  between  $L_P\_Center$  and  $L_S$ , edge effects were reduced, and the slab thickness was taken into account. After the energies were calculated,  $L_P$  was rotated to the next rotation (R) position and the above process was repeated until all R positions had been calculated at which point the data was saved and the run terminated.

Step sizes in the z-direction were computed dynamically in order to find the energy minimum for  $E_{int}$ . This allows for a minimum number of steps to be taken to reach the minima. Equation 4 describes how the step

size ( $\delta Z$ ) is calculated by taking the energy difference between steps into account ( $\delta E_{int}$ ) and using a size constant ( $S$ ) to control the smallest possible step size. Run termination occurs when  $\delta E_{int} < 0.001$  kcal mol<sup>-1</sup> and  $\delta Z < 0.001$  Å. Further details of how this algorithm is implemented are detailed in Figure S3.

$$\delta Z_i = S \log \left( \left| \frac{\delta E_{int}}{\delta Z_{i-1}} 10^3 \right| \right) \quad \text{Equation 4}$$

All unique combinations of predicted non-equivalent facets with a reasonable % total facet area representation (>1%) were tested. It is important to note that the calculations were not repeated with an inversion of L<sub>P</sub> and L<sub>S</sub> due to a negligible energy difference when swapping the probing layer for the substrate layer, i.e. 10-1/110  $\approx$  110/10-1 (as shown in Figure S4).

#### Data Analysis

Convergence data was processed separately using Origin Pro 2018<sup>22</sup> to fit the data. A python (3.6) tool has been developed to quickly, reliably, and consistently analyse the model output ([gitlab.com/alexamc/ssimtool](https://gitlab.com/alexamc/ssimtool)). Briefly, the SSIM Tool reads in the outputs of the SSIM calculations, converts the energy from kcal mol<sup>-1</sup> to mJ m<sup>-2</sup> (details in Equation S1), normalizes energies to the reticular area and handles the aggregation of datasets to allow for easier analysis of surface interactions. The tool also has built in graphing features allowing the users to plot energy distributions and spatial-energy data.

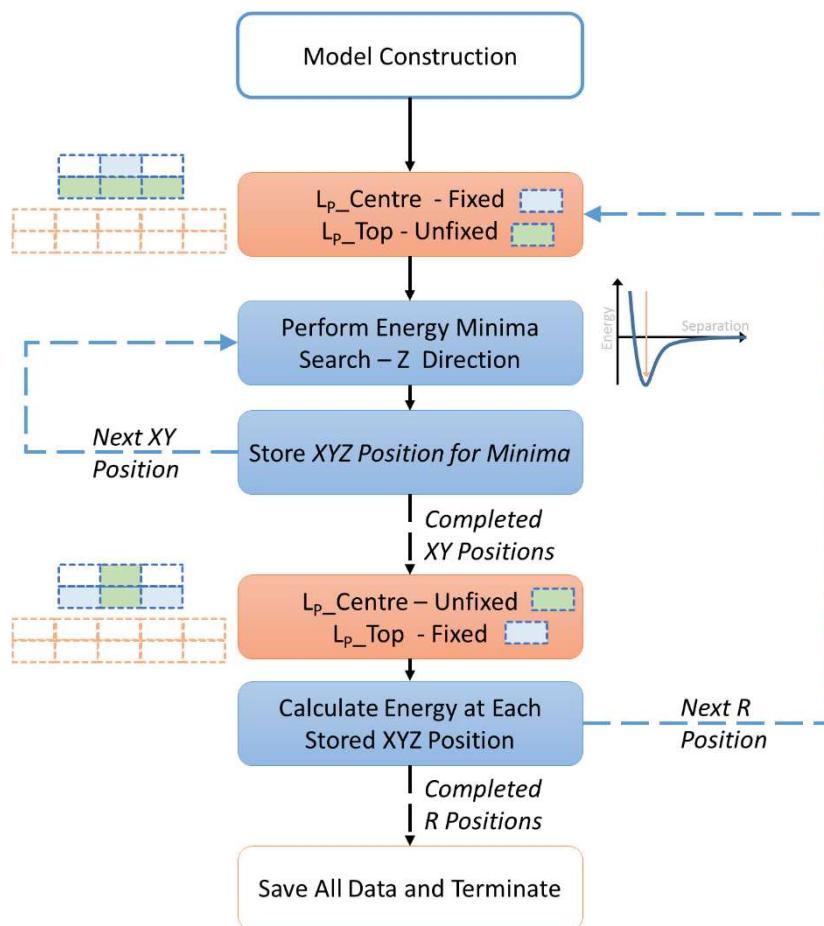


Figure 3 - Flow chart illustrating the steps involved in the calculation of the interaction energy between two surfaces across multiple XYZR positions.

The Pandas<sup>23</sup> and Seaborn<sup>24</sup> python libraries were used to generate violin plots, heatmaps, and separation energy distributions.

#### Convergence Data

Convergence tests were carried out to ensure the distances and sizes used for all surfaces and limiting radii were satisfactory for an accurate representation of the forces involved since the comparisons made between facets are relative and not absolute.

#### Limiting Radius

In order to determine the limiting radius for calculating the atom-atom interactions the energy between two parallel surfaces was calculated whilst the limiting radius was increased. Due to the lack of a periodic

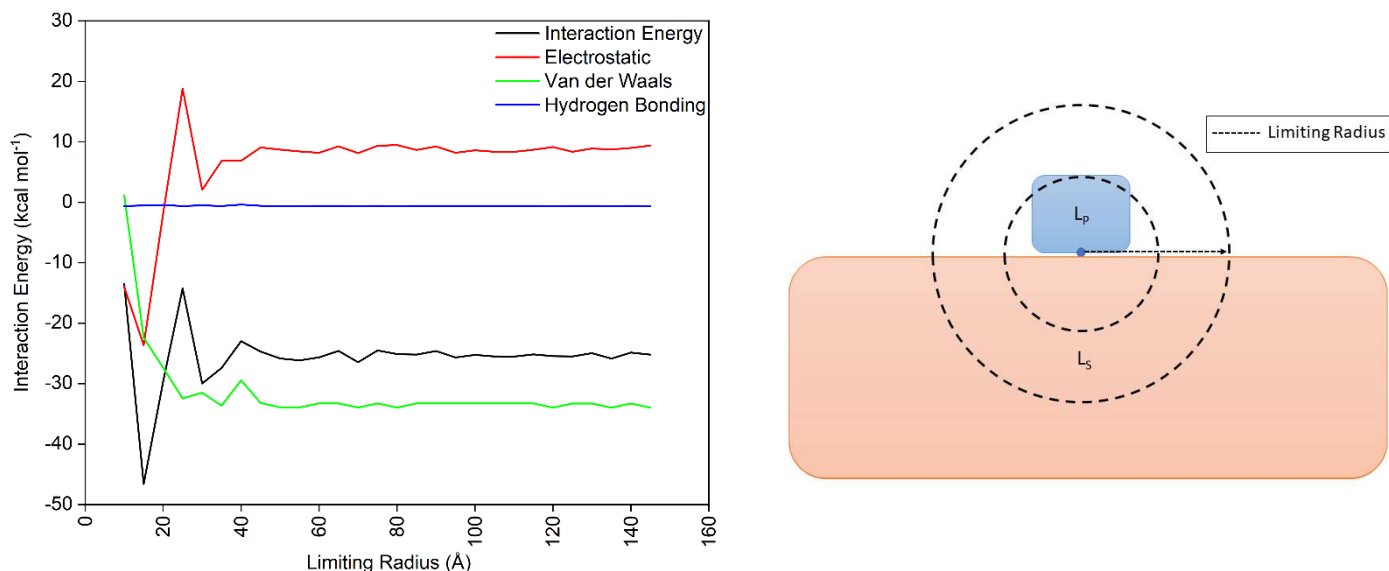


Figure 4 – Interaction energy of a system with a variable limiting radius, showing the behavior of different energy components. Illustration is provided to indicate which limiting radius the figure is referring to.

boundary, a large limiting radius of 80 Å was chosen based on the plateau of the interaction and electrostatic energy terms in Figure 4.

#### Layers Area and Thickness

$L_P$  was kept at a constant thickness of one d-spacing while the area of  $L_S$  was changed from 985 Å<sup>2</sup> to 10,905 Å<sup>2</sup> by incrementally increasing the number of repeating units using the  $U_s$  and  $V_s$  parameters. Using a convergence tolerance of 0.1 kcal mol<sup>-1</sup> for the difference in mean interaction energy between  $L_S$  and  $L_P$  across one set of X/Y scans, Figure 5A shows the minimum size of  $L_S$ , converging at approximately 3500 Å<sup>2</sup>. Convergence criteria are illustrated using dashed lines on each graph.

With the selected area, the thickness of  $L_S$  was increased while  $L_P$  was kept constant. This tested the minimum required thickness for  $L_S$  to account for most significant interactions.

The thickness of  $L_S$  was set to 36 Å (based on a convergence tolerance of 0.1 kcal mol<sup>-1</sup>), and  $L_P$  thickness was varied, as shown in Figure 5. A thickness of 36 Å was selected for both probe and substrate layer, based on the convergence data shown in Figure 5B and 5C). This thickness works well for the neutrally charged single component paracetamol structure. However, it can be expected that for any charged systems, such as salts, a larger thickness may be required. Therefore, we recommend new convergence testing is carried out when working with new systems.

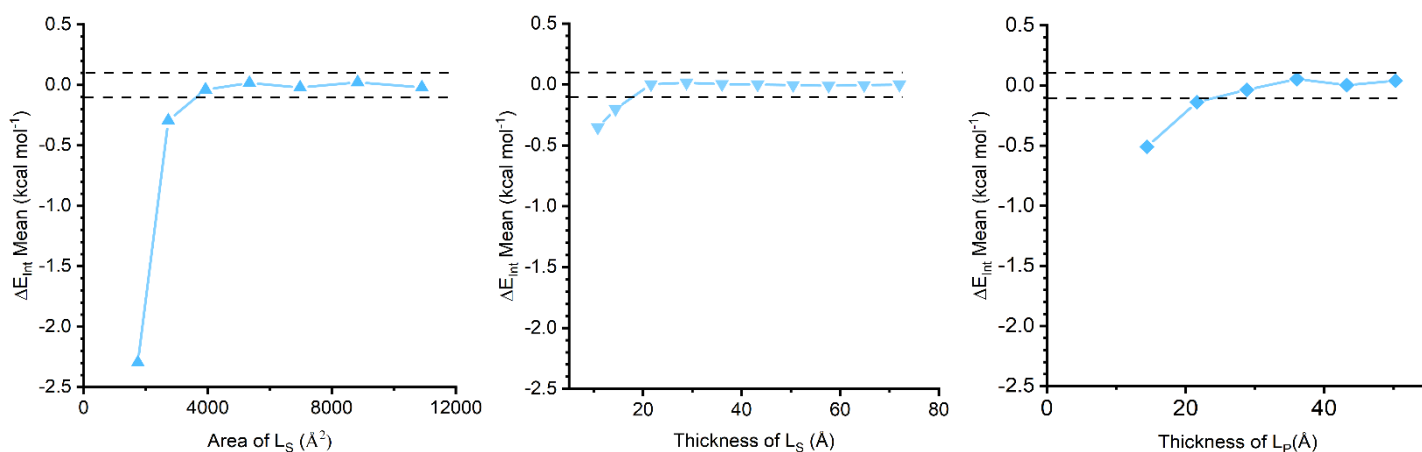


Figure 5 - Convergence plot of: A) increasing the area of  $L_S$  whilst  $L_P$  thickness is kept constant; B) increasing the thickness of  $L_S$  whilst  $L_P$  thickness is kept constant; C) increasing the thickness of  $L_P$  whilst  $L_S$  is kept at constant thickness. Dashed lines show the convergence criteria of the interaction energy at 0.1 kcal mol<sup>-1</sup>.

## Results and Discussions

Before the interactions between crystal surfaces can be studied, the molecular organisation of the crystal, as well as the overall crystal morphology, must be generated, optimized, and validated.

### Lattice and Morphology

The lattice energy of paracetamol form I, calculated with Dreiding and MOPAC as described in the Geometry Optimisation and Morphology Prediction section, was found to be  $-26.08 \text{ kcal mol}^{-1}$ , in good agreement with previously reported values for the enthalpy of sublimation ( $28.26 \text{ kcal mol}^{-1}$ )<sup>19</sup>. The contributions from each energy component were also calculated with 53.8% ( $-14.05 \text{ kcal mol}^{-1}$ ) from van der Waals, 23.9% ( $-6.25 \text{ kcal mol}^{-1}$ ) from electrostatics and 22.15% ( $-5.77 \text{ kcal mol}^{-1}$ ) from H-bond interactions.

The paracetamol morphology predicted with the attachment energy model exhibits a prismatic shape with dominant forms  $\{011\}$  and  $\{101\}$  accounting for 46% and 18% of the surface area of the crystal, respectively as shown in Table 1. The overall habit is similar to that reported elsewhere<sup>25,26</sup> however extensive modelling work by Beyer *et al.* suggests that  $\{110\}$  is the slower growth facet<sup>26</sup> and hence the major face. It is clear from the morphology data shown in Figure 6 that the  $\{011\}$  facets are substantially larger, covering 46.5% of total facet area, compared to the  $\{002\}$  facets which are much faster growing and represent less than 0.1% of the total facet area. It is important to note that these calculations are made in the absence of a solvent or any

Table 1 Morphology prediction based on the attachment energy model. Showing the facets, the number of times they occur (multiplicity) and their associated morphological data.

<b>hkl</b>	<b>Multiplicity</b>	<b><math>d_{hkl}</math></b>	<b>Attachment Energy (<math>\text{kcal mol}^{-1}</math>)</b>	<b>Slice Energy (<math>\text{kcal mol}^{-1}</math>)</b>	<b>% Total facet area</b>	<b>Anisotropy Factor %</b>
{ 0 1 1 }	4	7.206	-11.49	-15.76	46.528	60.43
{ 1 0 1 }	2	5.811	-11.95	-15.30	18.368	58.67
{ 1 0 -1 }	2	6.600	-13.31	-13.94	14.911	53.45
{ 0 2 0 }	2	4.682	-13.45	-13.80	4.065	52.91
{ 1 1 0 }	4	5.789	-14.23	-13.02	11.191	49.92
{ 1 1 -1 }	4	5.395	-14.57	-12.68	4.861	48.62
{ 0 0 2 }	2	5.642	-17.90	-9.35	0.075	35.85

supersaturation and thermal effects. These predictions assume vapor growth and are unlikely to be consistent with observed morphologies grown from solvents, though the major faces are present. As such, experimentally grown crystal habits might differ from the predicted morphology<sup>25</sup>.

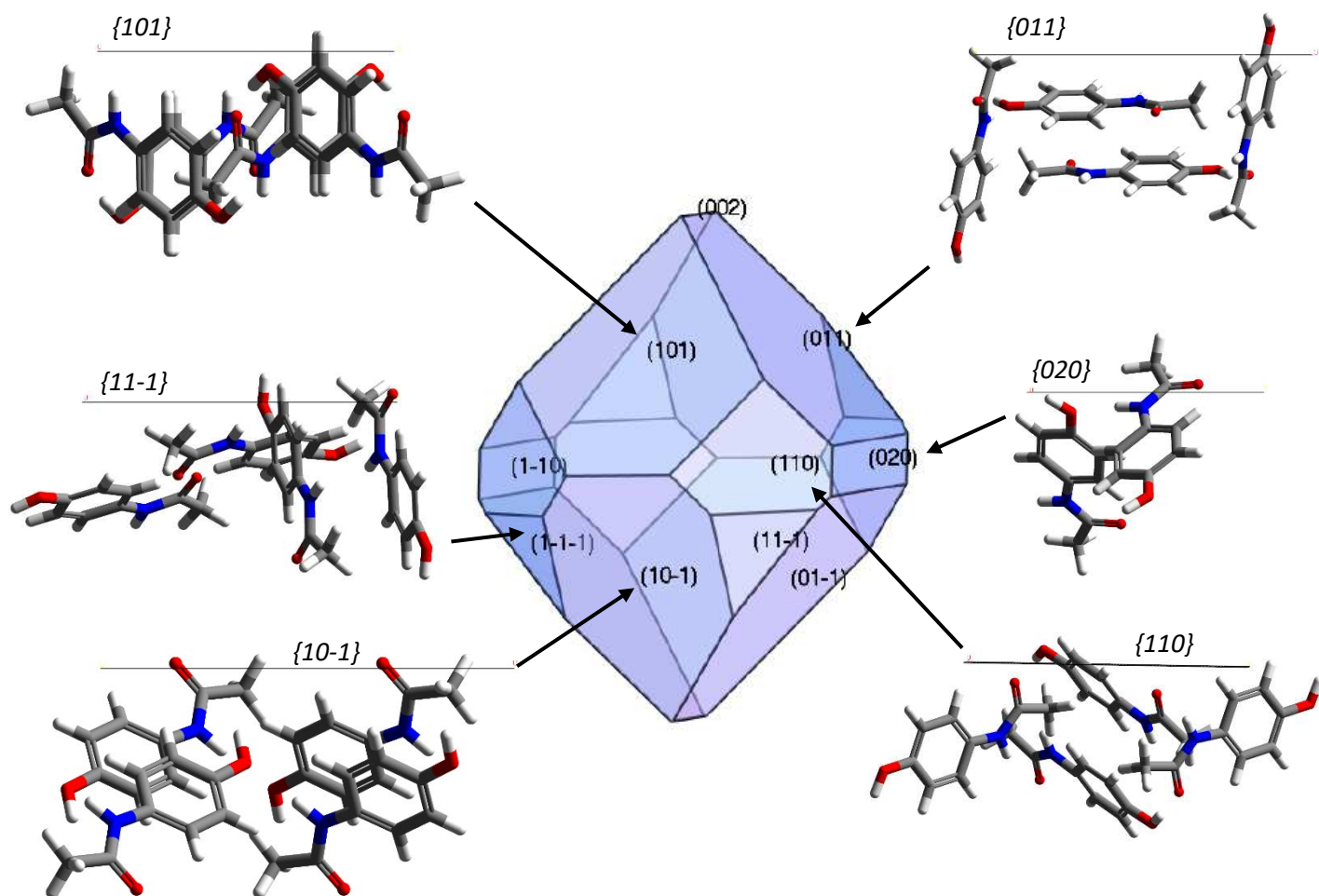


Figure 6 - The predicted morphology of paracetamol form I based on the attachment energy model. Also shown is the molecular structure at each surface. The most dominant facets are shown to be  $\{011\}$  and  $\{101\}$ . The black line on each facet indicates the Miller plane position defining the surface termination.

## Surface-Surface Interactions

The purpose of the surface-surface interaction model (SSIM) is to map the interaction of faceted organic crystals interacting cohesively (interactions occurring between similar materials) and adhesively (interactions occurring between different materials).

To achieve this, interactions at the atomistic scale are calculated across all possible positions with three degrees of translational and one of rotational freedom (XYZR) thereby providing a comprehensive description of the interaction energy distribution between two parallel faces. The influence of functional groups on the surface-surface interactions can be seen for the most stable positions and more generally as a function of the orientation. This data can be used as an input to process models describing operations such as flow, mixing/blending, and granulation, where both the optimal interaction energies and the averaged interaction energies are significant.

The following data (except the singular profile) was generated and analysed using the developed SSIMTool Python library which allows for consistent and fast data analysis.

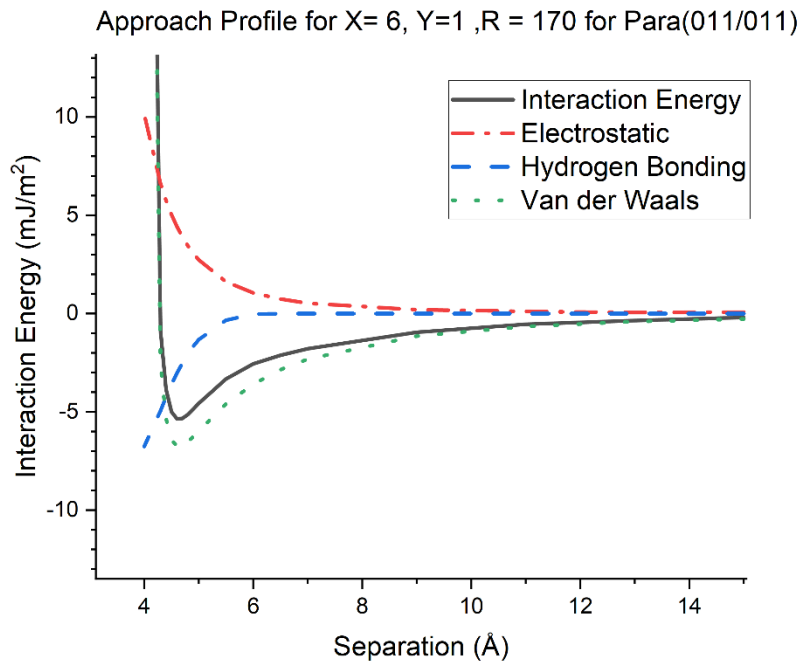


Figure 7- Energy Profile of probing layer (paracetamol [011],  $L_P$ ) approaching substrate layer (paracetamol [011],  $L_S$ ) at origin offset (6,1) and rotation of  $170^\circ$ . In this example, the total energy minimum occurs at  $\sim 4.4 \text{ \AA}$ , representing the distance between the miller planes caused by a steric interaction of opposing more prominent surface groups.

#### Approach Profile

Once all facet combinations have been calculated, several analyses can be performed. Firstly, single position (XYR) energy profiles as a function of the separation distance between the layers can be extracted, as shown in Figure 7. As the two surfaces approach each other, the interaction energy becomes more negative, indicating a dominating attractive region is reached, thereafter Pauli repulsive forces dominate. The bottom of the energy well is the energy minimum ( $E_{\min}$ ) where the optimum separation of the two layers is reached, and the depth of the energy well indicates the magnitude of the adhesive interaction, more negative being a stronger interaction. When using the Dreiding forcefield, the total interaction energy can be partitioned into its individual components: van der Waals, electrostatic, and H-bond interactions. This provides an indication of the relative importance of the different interactions between surfaces and can highlight areas where, for example, electrostatics dominate due to ion pairs interacting between two facets.

## Spatial Data

As the model stores the energy minima for all of the XYR positions, it is possible to analyse the exact mapping of this spatial displacement between the two slabs. Figure 8 shows the interaction energy minimum (left) at every XY position in the scanned grid between the two surfaces of 011/10-1. Values of strong total energy ( $\text{kcal mol}^{-1}$ ) are represented in blue in Figure 8 (left) correlating with the red regions in Figure 8 (right), illustrating the small separation between the surfaces and thus indicating interlocking. At a specific rotation, the two surfaces are more likely to interlock when shifted by 4 Å in the Y-axis, illustrated by the inverse relationship between the total energy and  $L_P$  z-axis displacement where the energy is significantly higher when  $L_P$  is closer to the substrate.

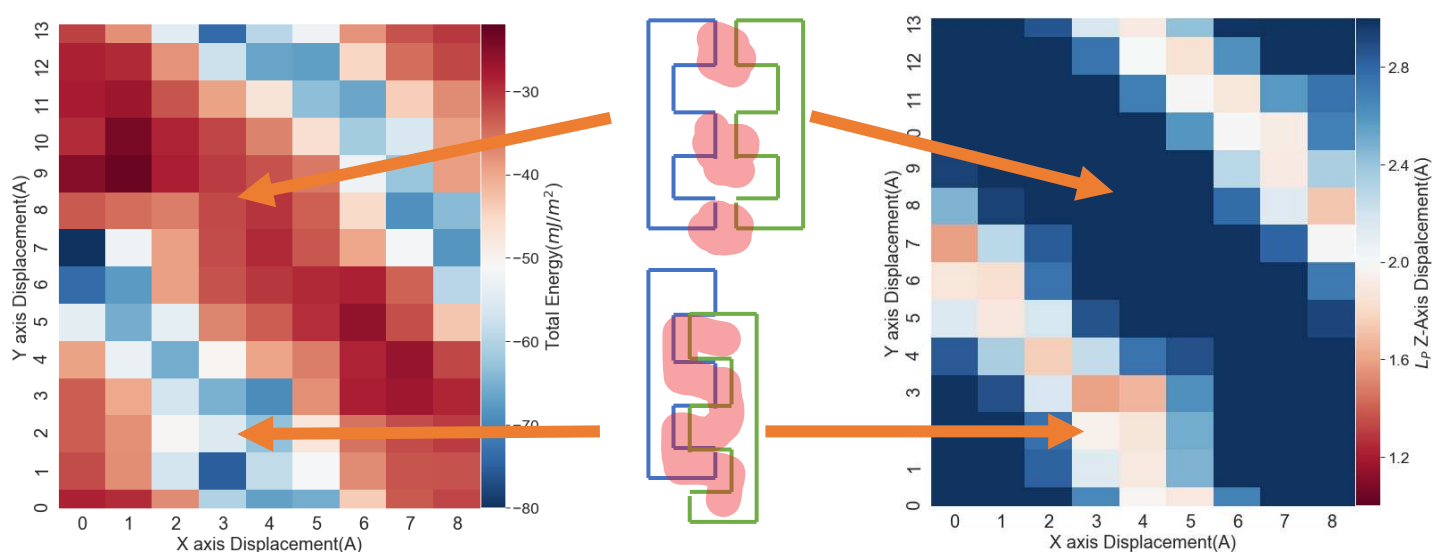


Figure 8 - Spatial energy plot showing the energy minima with every XY displacement of  $L_P$  for Para/Para-011/10-1 at a rotation of  $30^\circ$ , illustrating the separation function for the Total Energy of the interaction. Left) Total interaction energy at each XY position, with blue indicating a higher interaction energy. Right) The z-axis displacement of  $L_P$  for each XY position, with red indicating small separations between the two slabs. Interdigitation of the opposing lattices allows a small separation which results in a high energy.

## Distribution Data

Plotting distributions of all energy minima calculated for specific facets, across all rotations with  $5^\circ$  increments and 1 Å grid spacing, gives an indication of which facets interact most strongly and what range of energies exist within the system. In order to visualise all the facets simultaneously, the distributions are displayed as violin plots. These vertically plotted distributions show the full spread of calculated interaction

energies, from the average position out to the low probability minimum and maximum values. The violin plot for each facet is shown side by side on the same scale for direct comparison.

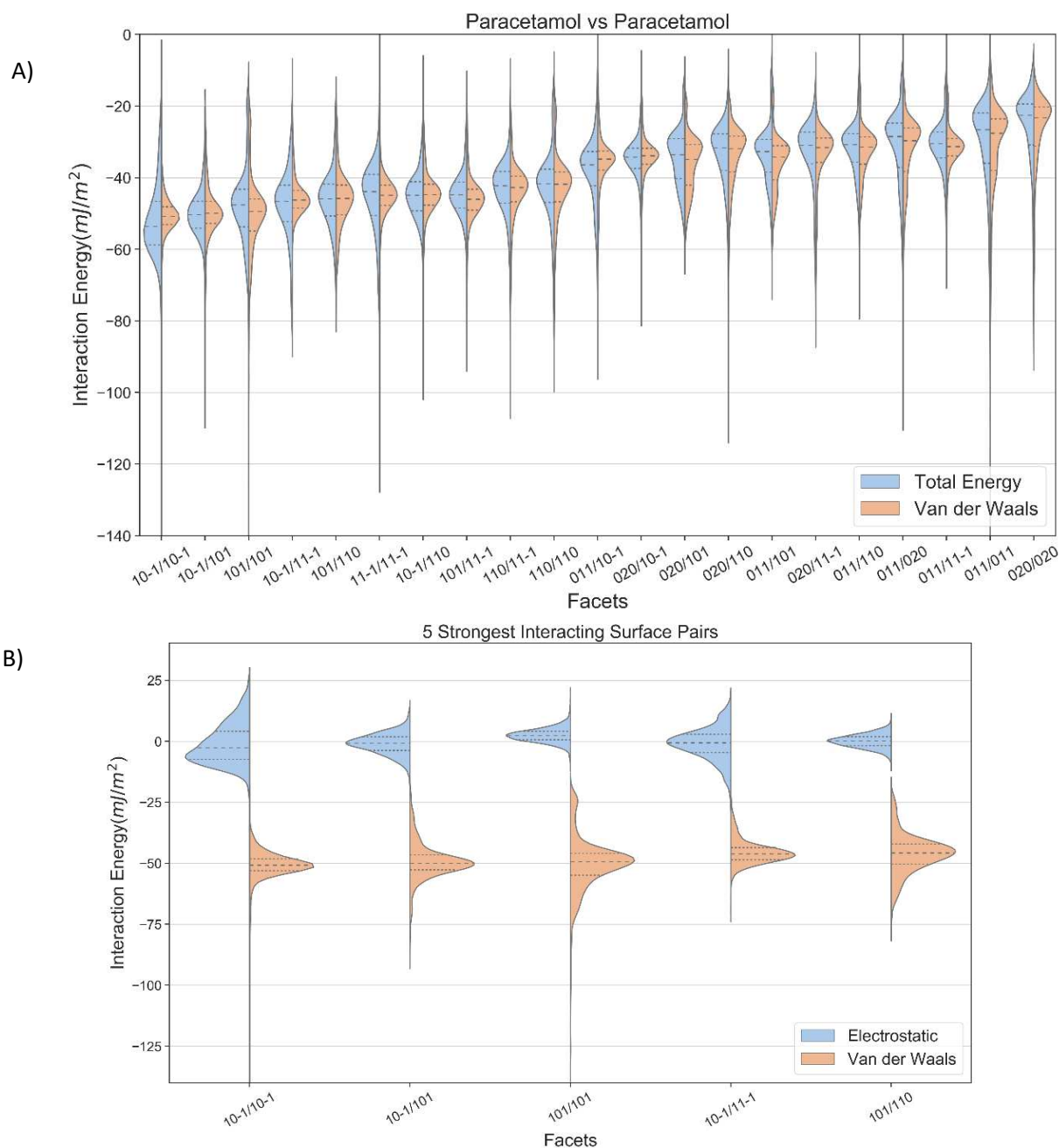


Figure 9 – A) Violin plots of Paracetamol with Paracetamol facet interaction distributions. Vertically plotted kernel density estimate plots show the Total Energy (blue) alongside the van der Waals energy component (orange). The distributions for each facet have been sorted by descending interaction energy based on the median energy. Dashed lines represent the mean and quartiles of the distributions. B) The component energies of the total interaction energy are displayed as Electrostatic (blue) and Van der Waals (orange) for the 5 strongest interacting surface pairs.

Figure 9A shows the different energy distributions across all facet pairs of Para/Para interactions. The total interaction energy (blue) is plotted alongside van der Waals energy (orange) to illustrate what proportion of the total energy is composed of vdW interactions. The vdW interactions accounts for more than 80% of the total interaction energy due to the fact both layers are neutral in charge (a graph illustrating this can be seen in Figure S5).

The 10-1/10-1, 011/011 and other homogeneous facet (like facets) pairings have a broad spread of interactions, -6 to -304  $\text{mJ m}^{-2}$  and -12 to -139  $\text{mJ m}^{-2}$  respectively. Such ranges are to be expected for like faces since at a particular point on the grid the interaction energy can be close to that of the energy of the lattice as the two surfaces align in such a way that a partial lattice continuation exists.

Figure 9B illustrates the range of energy from the contributing components. At the minimum, the contributing energies are balanced to achieve the lowest energy. As expected, the electrostatic component encompasses both attractive and repulsive values. The 10-1/10-1 surface shows an asymmetric distribution with the majority of electrostatic values calculated as attractive. This can be explained by the interaction between the carbonyl and hydroxyl groups present on this surface, as seen in Figure 6.

Previous approaches<sup>12</sup> to understanding particle-particle interactions have utilised a single energy point characterisation, with the strongest interaction value used to describe the interaction between the two systems (i.e. a crystal face and single molecular probe as a proxy for the second face). The logic behind this approach is that from a thermodynamic point of view the systems will favor the lowest energy position (a 3D energy well). This single point representing the strongest interaction would be equivalent to the most negative (lowest) point on the violin plot distributions in Figure 9. Whilst overall there is a general correlation with the average interaction energy of facets from left to right, the individual values of strongest interaction energy vary significantly from facet to facet.

Whilst the single energy point approach is valid for individual molecules adhering to surfaces, as they are not immediately integrated into the lattice but migrate over the crystal face until they find a favorable site for attachment, it is not applicable to the interactions of particles due to their significantly larger size and complex surface structure leading to an atomically rough surface that can cause steric hindrance and reduce the accessible contact area. Due to computational constraints we describe surfaces as pristine infinite repeats of a

unit cell. The reality is that the real faces of crystals are often also topographically rough. The roughness at this larger scale is caused by the specific growth mechanism for each individual face leading to surfaces with steps and kinks. At the still larger macroscopic scale, collision between individual crystals or between the crystal with the impeller lead to crystal breakage and thus macroscopically rough surfaces. Therefore, using a single energy point to describe the characteristic surface-surface interactions between individual particles in a powder could lead to overestimating the strength of the interactions. For example, such an energy point can be found with the strongest Para/Para interaction between 10-1/10-1, circled in orange in Figure 10.

Briefly, Figure 10 allows us to assess the distribution of interaction energy (right histogram), z-displacement of  $L_P$  (top histogram) and the relationship between the two. Zero displacement refers to when the two planes that define the surface termination are at the starting position, where the separation between the planes is 0 Å along the z-axis. Values that are observed towards the bottom left indicate a strong interaction energy and close proximity between the two surfaces.

As described previously, it is possible to align the slabs in such a way to get a *pseudo*-continuation of the crystal structure. Utilising the data sets described above it is possible to explain this result. Figure 10 also indicates the presence of a few positions that are outside the normal distribution of interaction energy, in particular the point that occurs at  $-300 \text{ mJ m}^{-2}$  while the median value is  $-55 \text{ mJ m}^{-2}$ . While this is an extreme example and would be described as an outlier considering it is part of 5,000 data points, it helps illustrate the point as these instances will exist for all homogenous surface interactions.

The linear regression fit shows us the relationship between the displacement of  $L_P$  and interaction energy. Typically, the interaction energy will be stronger when the displacement is smaller, and this is determined by the topological compatibility of the opposing surfaces. As the surfaces move closer, resulting in higher surface contact, the interaction energy increases.

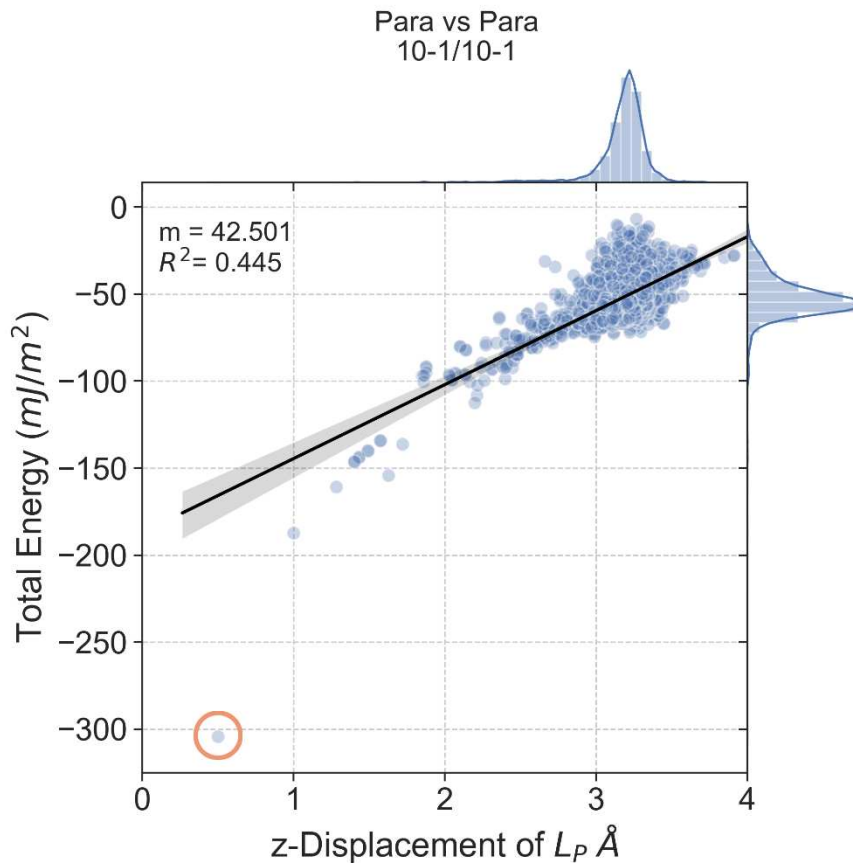


Figure 10 - Energy-separation plot of the Para10-1/10-1 face interactions. The histogram on the right hand axis shows the distribution of interaction energy, whereas the top horizontal distribution highlights the density of the displacements for  $L_P$ . A linear regression (black line) is fitted across the whole dataset to check for any correlation between the two values. Each energy at a given  $z$ -displacement is from a  $XY$  translation and  $Z$  rotation position. The orange circle highlights the strongest interaction outside the normal distribution of energy and displacement, which relates to a pseudo-continuation of the crystal structure.

## Energy-Separation Data

Most surface-surface interactions are driven by a distance component, where surfaces that can interlock or achieve a small separation have a stronger interaction energy due to their ability to form more contact points; the topology of the surface has a significant impact on the interaction energies.

However, in some instances an increase in interaction energy can be seen when the slab separation remains constant. We conjecture that the increase in energy is attributed to the compatibility in surface chemistries. This effect can be plotted using energy-separation diagrams as seen in Figure 11.

Plotting the displacement of  $L_P$  with its associated minimum energy value, it is possible to determine if topological or chemical features predominantly drive the interaction energies between two surfaces. In Figure 11, Para 020/020 shows an increase in interaction energy as the displacement is reduced, demonstrated by the wide distribution at the top of the plot. Para 10-1/11-1 shows a similar range of interaction energies, but the displacement of  $L_P$  is distributed around 3 Å, demonstrated this time by a narrow distribution.

Approximating the difference in energy per difference in displacement allows us to demonstrate the impact of the surface chemistry. For the 020/020 facets a total energy of  $\delta \sim 17 \text{ mJ m}^{-2} \text{ \AA}^{-1}$  can be calculated whereas the 10-1/11-1 facets result in  $\delta \sim 130 \text{ mJ m}^{-2} \text{ \AA}^{-1}$ .

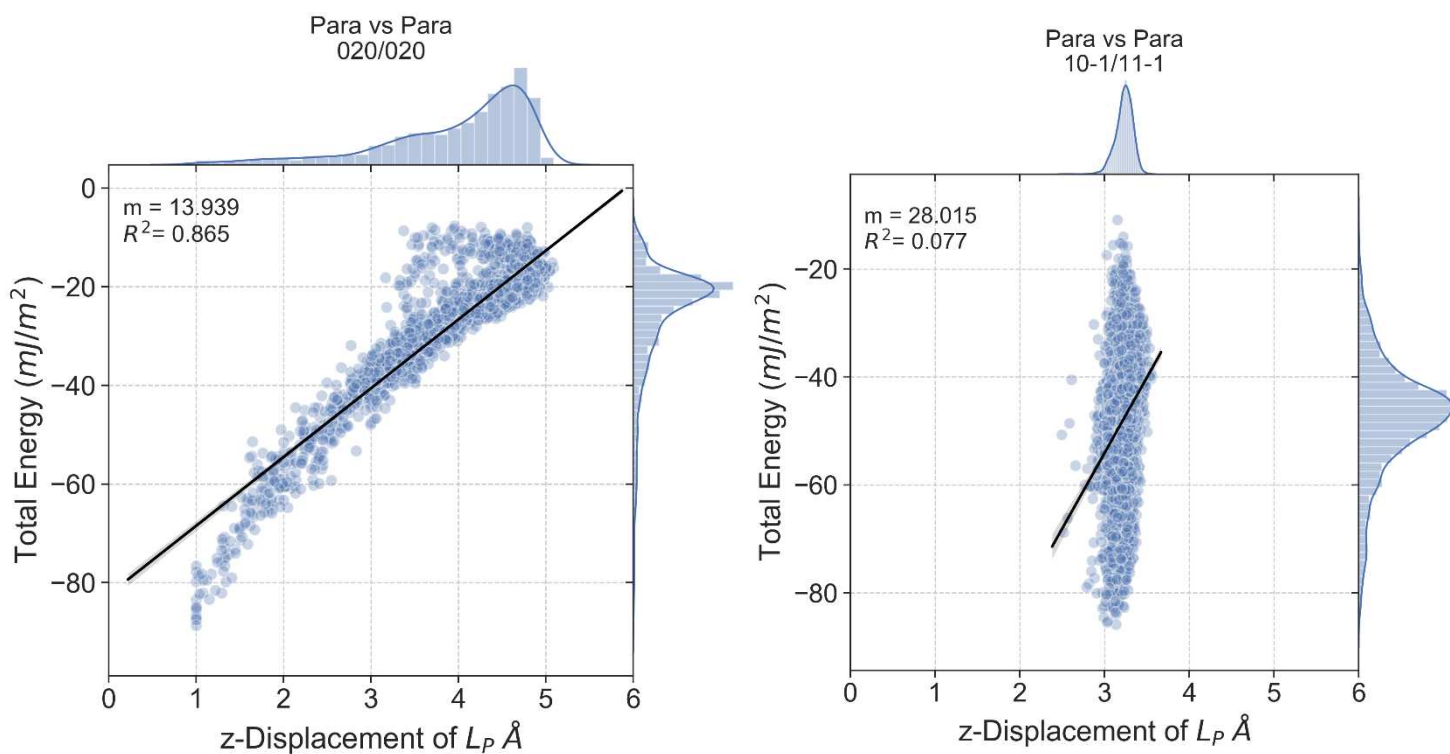


Figure 11 - The distribution of energy minima for homogeneous (left) and heterogeneous (right) surface pairs.

Fitting a linear regression allows for a quantitative comparison to be carried out across the dataset. When a topological feature dominates the interactions, the  $R^2$  value is higher (0.865 for Para 020/020) whereas for a more chemically driven interaction the opposite is true (0.077 for Para 10-1/11-1). With a reliable linear fit

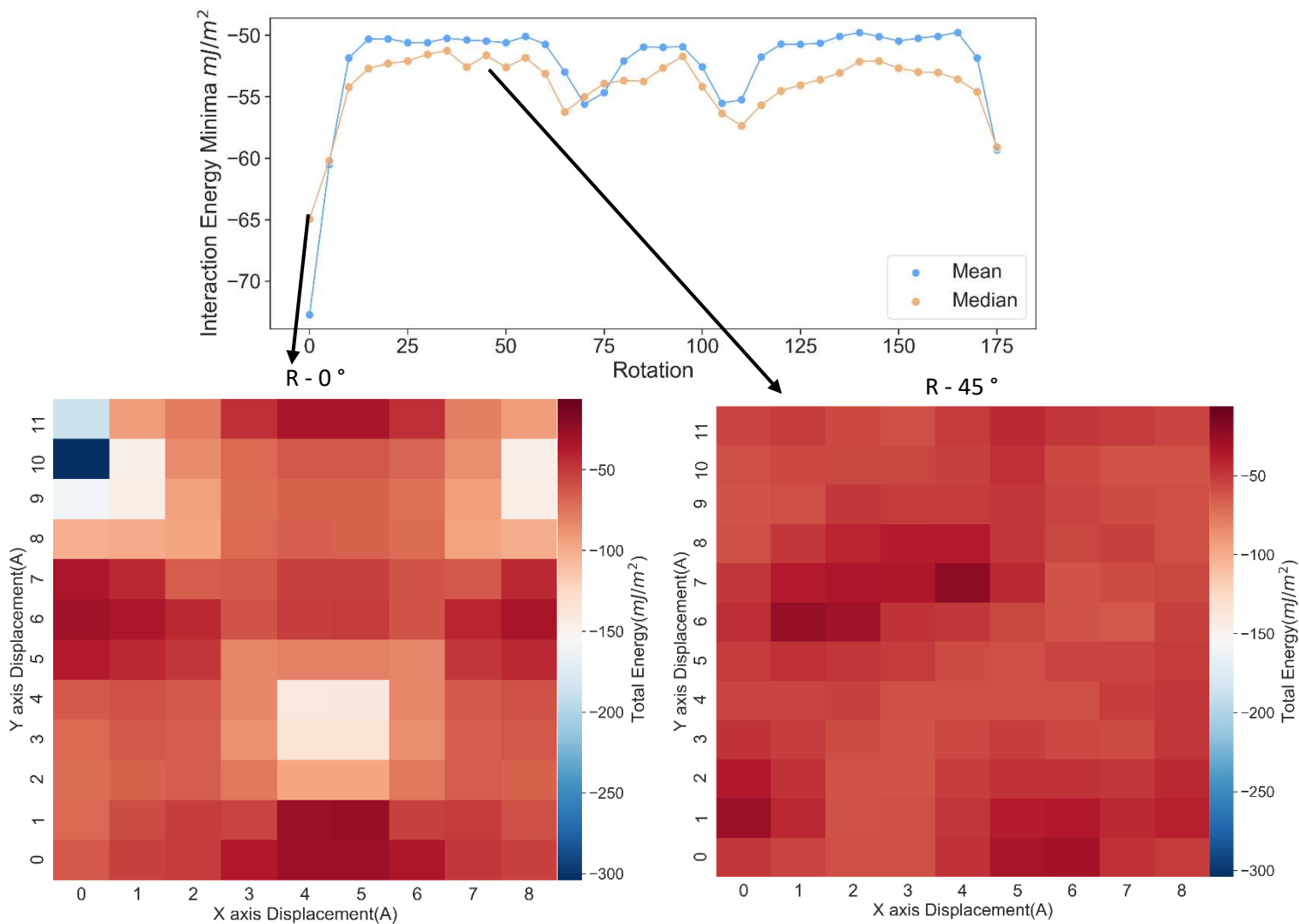


Figure 12 - Minima energy distribution for x, y spatial points whilst scanning through different rotations of LP.

Showing the specific point ( $x = 0, y = 10, R = 0$ ) at which the energy is much larger than the rest of the scans.

the gradient can indicate the magnitude of the increase in energy as a function of the displacement; the larger the gradient, the higher the interaction energy will be when the two layers are closer.

Surfaces with higher atomistic roughness tend to have lower interaction energies due to their reduced accessible surface area. However, in the presence of some specific surface features such as grooves or channels the range of interaction energies has a large spread due to surfaces interlocking at specific rotations. Plotting the mean and median values of the interaction energy minima across different rotations for the Para10-1/10-

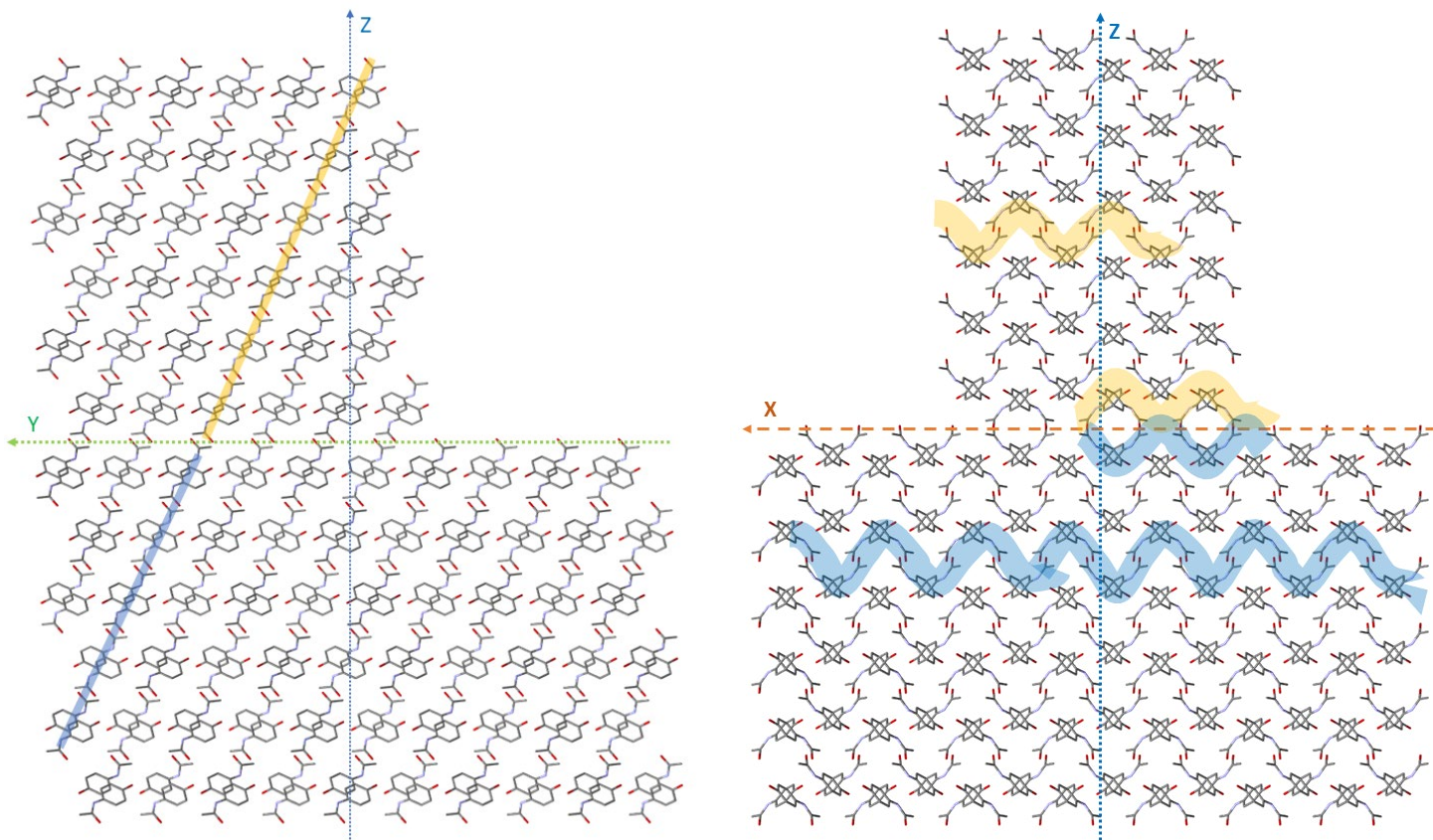


Figure 13 - Position of Para 10-1/10-1 at points (0,10,0 of x, y, r) as highlighted in Figure 12. A) Shows  $L_P$  interacting with  $L_S$  along the x-axis. Highlighted in blue are the aromatic ring chains within  $L_S$  aligned with the same groups in  $L_P$  (yellow). B) View along the y-axis, showing the mirror symmetry of the two slabs along the x-axis. Both figures illustrate how the single position can exhibit a continuation of the lattice from the bulk.

1, as shown in Figure 12, it is possible to identify a rotation at which there is a large singular interaction energy due to the large difference in the median and mean, indicative of an asymmetric distribution.

The spatial data gives the coordinates of the  $L_P$  with the interaction energy, which can be used to visualise the two layers and their exact positions as shown in Figure 13. The aromatic ring chain in  $L_P$  (highlighted yellow) can be seen continuing through the matching chain (blue) in  $L_S$ . However, the structure in Figure 13B) shows that it is not a complete lattice as a mirror plane exists along the y-axis, illustrated by the mirrored highlights on the interface.

#### Ranking Interactions

The average interaction energy along with the associated standard error for each probe is shown in Figure 14 (tabulated data can be found in Table S2), plotted against the anisotropy factor (Table 1). The anisotropy factor describes the degree of saturation of the intermolecular bonds on the surface and thus can be associated

with the potential activity of the surface. Para 10-1 has the highest average energy against all other facets but also the largest standard error indicative of the wider distributions.

Previous work<sup>21,27-30</sup> has suggested the use of the anisotropy factor to indicate which surfaces might interact more with other facets. However, SSIM suggests that there is more to the puzzle. Whilst there is some agreement, with both SSIM and anisotropy factor ranking {011} as the least interactive surface, the order of ranking is not consistent between the two models. Figure 14 shows the poor correlation between the two data sets. The {10-1} and {101} forms are calculated as the strongest interacting surfaces,  $-45.8 \text{ mJ m}^{-2}$  and  $-45.3 \text{ mJ m}^{-2}$  respectively. By contrast, the anisotropy factor ranks the {11-1} to be the most interactive (48.62%), whilst {10-1} and {101} as fourth and fifth most interactive. SSIM calculates the {11-1} to be third most interactive surface.

These results suggest that calculating surface-surface interactions across two crystal surfaces at all translational offsets and rotations can give a better indication of the cohesive particle properties within a particulate powder mixture. As this framework is designed to operate through the graphical interface as well

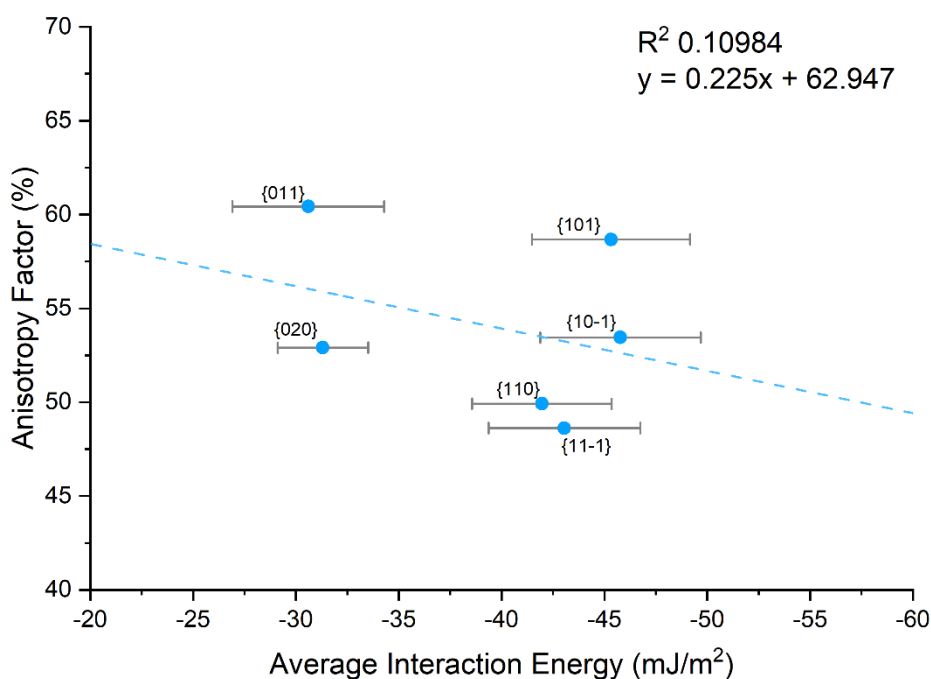


Figure 14 - Comparing the anisotropy factor calculated from the morphology prediction against the average interaction energy ( $\text{mJ m}^{-2}$ ). The linear fit (blue line) shows the poor correlation between the two datasets.

as scripts it is possible to automate inputs and use it on high performance computers, resulting in a high throughput calculation which can rank particle cohesive/adhesive behavior.

Furthermore, it is possible to weight the energies with the area representation, calculated from the morphology, to account for the probability of contact. Since smaller facets are less likely to interact than larger ones, multiplying the sizes of the facets as a percentage of the total particle size will yield expected interaction energy between two particles for each facet. With access to experimental data this tool can be tailored to model specific morphology and particle size distributions to ascertain the powders' cohesive or adhesive behavior.

Calculating the surface-surface interactions for a given number of facets found on two particles can inform other modelling techniques such as those used to model powder behavior and bulk properties. Quantified information about one particles affinity for another could be used to assess relationships in large systems.

Understanding the propensity for surfaces to interact with one another can offer vital information for controlling downstream processing within solid form formulations. Properties such as powder cohesivity impact agglomeration, punch sticking, drug delivery (particularly for inhalation formulations), and flowability. Whilst this model simulates systems under vacuum, it is possible to extend the application to include solvents that would represent systems at different humidity. Here we have presented the first step in quantifying the particle behavior using an automated system.

## Conclusions

We have shown the development of a computational framework that employs molecular mechanics in the calculation of surface-surface interaction energy distributions via a systematic method with four degrees of freedom. With the accompanying analysis tool the data can be accessed and processed to offer insight into the surface interactions through different plot types. Interaction energies between surfaces are considered in terms of distributions, providing a more holistic picture of all possible interaction configurations.

Using this method it is possible to get an overview of how all facets might interact between two particles to understand the cohesive and adhesive properties of a powder. The tool allows for the analysis of two specific surfaces in isolation, providing information about the relative importance of topological and chemical effects.

Distribution plots allow for an overview of each facet pair interaction, whilst the energy separation diagrams describe whether chemical or topological features drive the interactions. Utilising the spatial data, it is possible

to understand how the surface features of the two slabs complement each other and interlock to form strong interactions. Collating all the average data between all facets, it is possible to rank the facets in terms of their average interaction energy, weighted by surface representation, to understand how the particle would interact in general. Furthermore, this can be extended with the use of experimental data to describe the surface representation.

Using paracetamol as a test case, we have highlighted the importance of using distributions to describe the surface interactions and the pitfalls of using a single energy from a single surface configuration. Previous methods sought to use the lowest energy point (strongest interaction) to describe the propensity to adhere. Here we demonstrate that the lowest energy (strongest interaction) does not offer an accurate description of the likely surface interactions. We have described how the anisotropy factor does offer some agreement with the SSIM results, however, for paracetamol/paracetamol interactions the anisotropy factor does not account for topological induced steric hindrance of incoming surfaces and thus wrongfully ranks the most interactive surface

The presented method can be used to rapidly understand the influence of particle-particle interactions on pharmaceutical formulation, manufacturing, and product performance, reducing the time and resources required to deliver a drug to market.

## ACKNOWLEDGMENT

We would like to thank the HPC team at the University of Leeds, for their help and advice. Part of this work was undertaken on ARC3, part of the High-Performance Computing facilities at the University of Leeds, UK. A.A.M would like to thank the EPSRC CDT in Complex Particulate Products and Processes, Pfizer and CCDC for their generous funding of this work.

## ASSOCIATED CONTENT

Supporting Information listed as word document “Automated In-Silico Energy Mapping of Facet Specific Inter Particle Interactions Supporting Information.docx”, link to model script ([gitlab.com/AlexAMC/SSIM](https://gitlab.com/AlexAMC/SSIM)), and the analysis tool ([gitlab.com/AlexAMC/SSIMTool](https://gitlab.com/AlexAMC/SSIMTool)).

## AUTHOR INFORMATION

### Corresponding Authors

\*A.A. Moldovan – [amoldovan@ccdc.cam.ac.uk](mailto:amoldovan@ccdc.cam.ac.uk)

\*S.D.A. Connell – [s.d.a.connell@leeds.ac.uk](mailto:s.d.a.connell@leeds.ac.uk)

### Present Addresses

†A.A. Moldovan - Cambridge Crystallographic Data Centre, Cambridge, UK

### Funding Sources

EPSRC founding through the CPD in Complex Particulate Products and Processes EP/L015285/1.

## References

- (1) Lee, S. L.; O’Connor, T. F.; Yang, X.; Cruz, C. N.; Chatterjee, S.; Madurawe, R. D.; Moore, C. M. V.; Yu, L. X.; Woodcock, J. Modernizing Pharmaceutical Manufacturing: From Batch to Continuous Production. *Journal of Pharmaceutical Innovation*. 2015. <https://doi.org/10.1007/s12247-015-9215-8>.
- (2) Congdon, K. Inside Pfizer’s Modular Manufacturing PODs. *Pharmaceutical Online* **2015**, 4–6.
- (3) Blackwood, D. O.; Bonnassieux, A.; Cogoni, G. Continuous Direct Compression Using Portable Continuous Miniature Modular & Manufacturing. In *Chemical Engineering in the Pharmaceutical Industry: Drug Product Design, Development, and Modeling*; John Wiley & Sons, Inc.: Hoboken, NJ, USA, 2019; pp 547–560. <https://doi.org/10.1002/9781119600800.ch72>.
- (4) Burcham, C. L.; Florence, A. J.; Johnson, M. D. Continuous Manufacturing in Pharmaceutical Process Development and Manufacturing. *Annual Review of Chemical and Biomolecular Engineering*. Annual Reviews Inc. June 7, 2018, pp 253–281. <https://doi.org/10.1146/annurev-chembioeng-060817-084355>.
- (5) Chadha, R.; Bhandari, S. Drug-Excipient Compatibility Screening-Role of Thermoanalytical and Spectroscopic Techniques. *Journal of Pharmaceutical and Biomedical Analysis* **2014**, *87*, 82–97. <https://doi.org/10.1016/j.jpba.2013.06.016>.
- (6) Shah, U. V.; Karde, V.; Ghoroi, C.; Heng, J. Y. Y. Influence of Particle Properties on Powder Bulk Behaviour and Processability. *International Journal of Pharmaceutics*. Elsevier B.V. February 25, 2017, pp 138–154. <https://doi.org/10.1016/j.ijpharm.2016.12.045>.
- (7) Mangal, S.; Meiser, F.; Tan, G.; Gengenbach, T.; Morton, D. A. V.; Larson, I. Applying Surface Energy Derived Cohesive-Adhesive Balance Model in Predicting the Mixing, Flow and Compaction Behaviour of Interactive

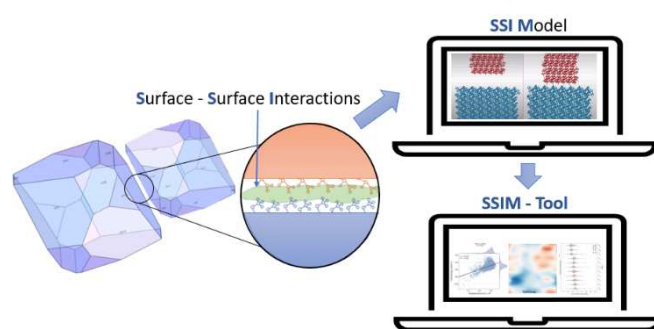
- Mixtures. *European Journal of Pharmaceutics and Biopharmaceutics* **2016**, *104*, 110–116. <https://doi.org/10.1016/j.ejpb.2016.04.021>.
- (8) Sun, C. C. Materials Science Tetrahedron - A Useful Tool for Pharmaceutical Research and Development. *Journal of Pharmaceutical Sciences*. John Wiley and Sons Inc. 2009, pp 1671–1687. <https://doi.org/10.1002/jps.21552>.
- (9) Yu, L. X. Pharmaceutical Quality by Design: Product and Process Development, Understanding, and Control. *Pharmaceutical Research*. Springer April 10, 2008, pp 781–791. <https://doi.org/10.1007/s11095-007-9511-1>.
- (10) Hammond, R. B.; Pencheva, K.; Roberts, K. J. Molecular Modeling of Crystal-Crystal Interactions between the  $\alpha$ - and  $\beta$ -Polymorphic Forms of L-Glutamic Acid Using Grid-Based Methods. *Crystal Growth and Design* **2007**, *7* (5), 875–884. <https://doi.org/10.1021/cg0605234>.
- (11) Hammond, R. B.; Jeck, S.; Ma, C. Y.; Pencheva, K.; Roberts, K. J.; Auffret, T. An Examination of Binding Motifs Associated with Inter-Particle Interactions between Facetted Nano-Crystals of Acetylsalicylic Acid and Ascorbic Acid through the Application of Molecular Grid-Based Search Methods. *Journal of Pharmaceutical Sciences* **2009**, *98* (12), 4589–4602. <https://doi.org/10.1002/jps.21758>.
- (12) Ramachandran, V.; Murnane, D.; Hammond, R. B.; Pickering, J.; Roberts, K. J.; Soufian, M.; Forbes, B.; Jaffari, S.; Martin, G. P.; Collins, E.; Pencheva, K. Formulation Pre-Screening of Inhalation Powders Using Computational Atom-Atom Systematic Search Method. *Molecular Pharmaceutics* **2015**, *12* (1), 18–33. <https://doi.org/10.1021/mp500335w>.
- (13) Hammond, R. B.; Pencheva, K.; Ramachandran, V.; Roberts, K. J. Application of Grid-Based Molecular Methods for Modeling Solvent-Dependent Crystal Growth Morphology: Aspirin Crystallized from Aqueous Ethanolic Solution. *Crystal Growth & Design* **2007**, *7* (9), 1571–1574. <https://doi.org/10.1021/cg070310u>.
- (14) Bak, J. M.; Dominiak, P. M.; Wilson, C. C.; Woniak, K. Experimental Charge-Density Study of Paracetamol - Multipole Refinement in the Presence of a Disordered Methyl Group. *Acta Crystallographica Section A: Foundations of Crystallography* **2009**, *65* (6), 490–500. <https://doi.org/10.1107/S0108767309031729>.
- (15) Groom, C. R.; Bruno, I. J.; Lightfoot, M. P.; Ward, S. C. The Cambridge Structural Database. *Acta Crystallographica Section B: Structural Science, Crystal Engineering and Materials* **2016**, *72* (2), 171–179. <https://doi.org/10.1107/S2052520616003954>.
- (16) Dassault Systèmes BIOVIA. Materials Studio. *Release 2017*. San Diego: Dassault Systèmes 2016.
- (17) Mopac. Quantum Chemistry Program Exchange Program. Indiana University: Creative Arts Building 181.
- (18) Dewar, M. J. S.; Zoebisch, E. G.; Healy, E. F.; Stewart, J. J. P. AM1: A New General Purpose Quantum Mechanical Molecular Model. *Journal of the American Chemical Society* **1985**, *107* (13), 3902–3909. <https://doi.org/10.1021/ja00299a024>.
- (19) Perlovich, G. L.; Volkova, T. V.; Bauer-Brandl, A. Polymorphism of Paracetamol. *Journal of Thermal Analysis and Calorimetry* **2007**, *89* (3), 767–774. <https://doi.org/10.1007/s10973-006-7922-6>.
- (20) Hartman, P.; Perdok, W. G. On the Relations between Structure and Morphology of Crystals. III. *Acta Crystallographica* **1955**, *8* (9), 525–529. <https://doi.org/10.1107/s0365110x55001680>.
- (21) Nguyen, T. T. H.; Rosbottom, I.; Marziano, I.; Hammond, R. B.; Roberts, K. J. Crystal Morphology and Interfacial Stability of RS-Ibuprofen in Relation to Its Molecular and Synthonic Structure. **2017**. <https://doi.org/10.1021/acs.cgd.6b01878>.
- (22) Corporation, O. Origin(Pro). Northampton, MA, USA 2018.
- (23) Wes McKinney. Data Structures for Statistical Computing in Python. In *Proceedings of the 9th Python in Science Conference*; 2010; pp 51–56.

- (24) Waskom, M.; Botvinnik, O.; Hobson, P.; Cole, J. B.; Halchenko, Y.; Hoyer, S.; Miles, A.; Augspurger, T.; Yarkoni, T.; Megies, T.; Coelho, L. P.; Wehner, D.; cynddl; Ziegler, E.; diego0020; Zaytsev, Y. V.; Hoppe, T.; Seabold, S.; Cloud, P.; Koskinen, M.; Meyer, K.; Qalieh, A.; Allan, D. Seaborn: Version 0.8.1. November 14, 2014. <https://doi.org/10.5281/zenodo.12710>.
- (25) Omar, W.; Al-Sayed, S.; Sultan, A.; Ulrich, J. Growth Rate of Single Acetaminophen Crystals in Supersaturated Aqueous Solution under Different Operating Conditions. *Crystal Research and Technology* **2008**, *43* (1), 22–27. <https://doi.org/10.1002/crat.200710995>.
- (26) Beyer, T.; Day, G. M.; Price, S. L. The Prediction, Morphology, and Mechanical Properties of the Polymorphs of Paracetamol. *Journal of the American Chemical Society* **2001**, *123* (21), 5086–5094. <https://doi.org/10.1021/ja0102787>.
- (27) Moldovan, A. A.; Rosbottom, I.; Ramachandran, V.; Pask, C. M.; Olomukhoro, O.; Roberts, K. J. Crystallographic Structure, Intermolecular Packing Energetics, Crystal Morphology and Surface Chemistry of Salmeterol Xinafoate (Form I). *Journal of Pharmaceutical Sciences* **2017**, *106* (3), 882–891. <https://doi.org/10.1016/j.xphs.2016.11.016>.
- (28) Bryant, M. J.; Rosbottom, I.; Bruno, I. J.; Docherty, R.; Edge, C. M.; Hammond, R. B.; Peeling, R.; Pickering, J.; Roberts, K. J.; Maloney, A. G. P. “Particle Informatics”: Advancing Our Understanding of Particle Properties through Digital Design. *Crystal Growth & Design* **2019**, *19* (9), 5258–5266. <https://doi.org/10.1021/acs.cgd.9b00654>.
- (29) Rosbottom, I.; Ma, C. Y.; Turner, T. D.; O’Connell, R. A.; Loughrey, J.; Sadiq, G.; Davey, R. J.; Roberts, K. J. Influence of Solvent Composition on the Crystal Morphology and Structure of P-Aminobenzoic Acid Crystallized from Mixed Ethanol and Nitromethane Solutions. *Crystal Growth and Design* **2017**, *17* (8), 4151–4161. <https://doi.org/10.1021/acs.cgd.7b00425>.
- (30) Rosbottom, I.; Roberts, K. J.; Docherty, R. The Solid State, Surface and Morphological Properties of p-Aminobenzoic Acid in Terms of the Strength and Directionality of Its Intermolecular Synthons. *CrystEngComm* **2015**, *17* (30), 5768–5788. <https://doi.org/10.1039/c5ce00302d>.

# Automated In-Silico Energy Mapping of Facet Specific Inter-Particle Interactions

*Alexandru A. Moldovan<sup>†,1,\*</sup>, Radoslav Y. Penchev<sup>‡</sup>, Robert B. Hammond<sup>§</sup>, Jakub P. Janowiak<sup>†</sup>, Thomas E.*

*Hardcastle<sup>†,1</sup>, Andrew G. P. Maloney<sup>1</sup>, and Simon D. A. Connell<sup>1,\*</sup>*



A surface-surface model was developed, in conjunction with an analysis tool, to compute possible particle-particle interactions between single organic crystals. We show how the tools can be used to find surface chemistry contributions, specific surface affinities, and roughness driven interactions, providing data for particle engineering problems.